NUMERICAL SIMULATION OF REFLECTOMETRY DENSITY MEASUREMENTS IN A REVERSED FIELD PINCH.

M. Brambilla, M. Moresco †

IPP 5/11 September 1986

MAX-PLANCK-INSTITUT FÜR PLASMAPHYSIK

8046 GARCHING BEI MÜNCHEN

MAX-PLANCK-INSTITUT FÜR PLASMAPHYSIK

GARCHING BEI MÜNCHEN

NUMERICAL SIMULATION OF REFLECTOMETRY DENSITY MEASUREMENTS IN A REVERSED FIELD PINCH.

M. Brambilla, M. Moresco †

IPP 5/11 September 1986

†Istituto di Elettrotecnica e di Elettronica
dell' Universitá di Padova, Italy

Die nachstehende Arbeit wurde im Rahmen des Vertrages zwischen dem Max-Planck-Institut für Plasmaphysik und der Europäischen Atomgemeinschaft über die Zusammenarbeit auf dem Gebiete der Plasmaphysik durchgeführt.

NUMERICAL SIMULATION OF REFLECTOMETRY DENSITY MEASUREMENTS IN A REVERSED FIELD PINCH.

M. Brambilla, M. Moresco †

†Istituto di Elettrotecnica e di Elettronica
dell' Universitá di Padova, Italy

Abstract.

The reflection of an Ordinary Wave from its cut-off at the electron plasma frequency can be exploited to measure the density profile of laboratory plasmas. We present two codes for the numerical simulation of broad band reflectometry on a Reversed Field Pinch.

The RAYRFP code evaluates the h.f. field distribution in the geometric optic approximation. It can rapidly simulate a frequency scan by evaluating the optical length of the "central" ray. It can also be used for example to estimate the angular spread of the reflected wave due to refraction and reflection from a cylindrical convex surface.

Because of the large shear characteric of Reversed Field Pinches, coupling between the ordinary and the extraordinary modes in the plasma can be important. Mode mixing is investigated by solving the full wave equation for nearly equatorial waves with a finite element code FELRFP. The results show that indeed a non negligible amount of power can be trasferred from the launched O-mode to the unwanted X-mode (or viceversa). Although stronger in small devices, this effect can also be substantial when the optical path is long, even in plasmas so large that the variation of $\vec{B}$ per wavelength is small. The mixing coefficient is found to be an oscillating function of frequency, indicating that the excitation of standing waves between the plasma edge and the cut-offs also plays a role. Nevertheless, the implementation of reflectometry should still be possible without difficulty in sufficiently large devices.

1. Introduction

Reflectometry exploits reflection of electromagnetic waves from cut-offs to measure the electron density of a nonuniform plasma. In the presence of a static magnetic field, the ordinary wave is reflected from the layer where the plasma frequency f_{pe} equals the wave frequency f; the extraordinary wave from the layers where $f_{pe}^2 = f^2 \pm f f_{ce}$, where f_{ce} is the electron cyclotron frequency. The position of the reflection layer can be deduced from the round trip delay time, or from the phase lag of the reflected signal. The former method has been extensively used in ionospheric plasmas [1], [2]; the latter is preferred in laboratory plasmas, where the delay time would be measured in nanoseconds [3]-[5].

The availability of microwave sources delivering adequate power over a large frequency range, and of broad-band microwave components, has recently increased the interest in this diagnostic for magnetically confined plasmas. By sweeping the frequency over several tens of Ghz, density profiles with excellent space and time resolution can be obtained, with several advantages over multichord interferometry: only one access port is needed; the microwave system is relatively simple; it is possible to measure the density down to a few centimeters from the plasma edge [6]. The working principle of a reflectometer is sketched in Fig. 1.

Wide-band reflectometry has been successfully implemented on the tokamaks TFR [7], [8], and Petula [9], and is planned for JET and Tore Supra. The present report adresses some questions which did arise during a preliminary study in view of its application on Reversed Field Pinches (RFP), in particular on the RFX device under construction at Padova [10].

The interpretation of reflectometry is in principle simple. The measured phase shift is given, within the WKB approximation, by

$$\Phi(f) = \frac{4\pi f}{c} \int_a^{r_c(f)} N(r,f)\,dr \qquad (1)$$

where $N(r,f)$ is the local refractive index, a the plasma radius, and $r_c(f)$ the cut-off radius for the frequency f. For the ordinary wave, $N(r,f) = (f^2 - f_{pe}^2(r))^{1/2}$; derivation of Eq. (1) with respect to f followed by Abel inversion gives the well-known formula for the cut-off position,

$$r_c(f) = \frac{c}{2\pi^2} \int_0^f \frac{d\Phi/df'}{(f-f')^{1/2}}\,df' \qquad (2)$$

which allows the reconstruction of the density profile from the derivative of the measured phase delay versus frequency, $\Phi(f)$. A correction $\delta\Phi$ arising near the reflection layer

($\delta\Phi \simeq \pi/2$, cfr. [2]) is easily taken into account. A more severe limitation comes from the fact that the lower limit of the frequency scan cannot easily be pushed below a few tens of Ghz: as a consequence, densities lower than a few times 10^{12} are difficult to probe.

No analytic inversion equivalent to Eq. (2) exists in the case of extraordinary wave launching: Eq. (1) has then to be inverted numerically [9]. Even for the ordinary mode, Eq. (1) is only valid for waves propagating strictly in the radial direction. The radiation pattern of an antenna, however, necessarily has a finite angular width; refraction, and reflection from a cylindrically convex surface will amplify the spread further. Hence the question arises how much of the reflected signal will reach the receiving antenna. Also, a wave propagating obliquely with respect to the minor plasma radius is reflected from a caustic displaced outwardly with respect to the theoretical cut-off: this introduces an incertitude in the reconstruction of the profile, in addition to those already mentioned.

Questions of this kind are conveniently investigated using a ray tracing code, which has been adapted for the present purpose from a ray tracing package previously developed to study Lower Hybrid and Ion Cyclotron resonance heating. This code will be described in the next Section, and a few examples of its use will be presented there.

A further class of questions is connected with the specific characteristics of the RFP equilibrium. From the point of view of h.f. wave propagation, the most important difference between a RFP and a Tokamak is that in the RFP the poloidal and toroidal components of the static magnetic field are of comparable magnitude, and the latter changes sign between the center and the edge of the discharge. As a consequence, shear is quite large, while toroidal effects can to a good approximation be neglected. A simple theoretical description of the RFP equilibrium, neglecting toroidicity, is the so-called Bessel Function Model (BFM) [11]:

$$B_\theta = B_o J_1(2\vartheta \frac{r}{a}) \qquad B_\phi = B_o J_o(2\vartheta \frac{r}{a}) \tag{3}$$

where a is the plasma radius, and $\vartheta = B_\theta(a)/\langle B_\phi \rangle$ is the pinch parameter (typically, $\vartheta \simeq 1.5$). Experimental profiles of B_θ and B_ϕ are shown in Fig. 2; the BFM is seen to be an excellent approximation in the central region, and somewhat poorer near the edge of the discharge [12].

The large shear characteristic of the RFP configuration is a source of coupling between the ordinary and the extraordinary mode of the uniform plasma [13]. The consequent loss of control over polarisation can be a nuisance for the straightforward interpretation of measurements. To investigate the importance of mode mixing under realistic conditions, we have written a code which solves the full cold plasma waves equations for h.f.

waves launched radially (i.e. with $m_\theta \simeq n_\phi \simeq 0$) into a cylindrical RFP described by the BFM equilibrium. This code, which uses Finite Element discretisation to avoid the problems associated with evanescent waves, is presented in Section 3.

The main result obtained is that mode mixing is not a serious problem at sufficiently low frequencies (below 80 - 90 Ghz in a device of the RFX size, $a = 40$ cm, $n(0) \simeq 2 \cdot 10^{14}$ cm^{-3}), but becomes indeed important when the optical path is long, or in smaller devices. We also find that the mixing coefficient is an oscillating function of the applied frequency, with period corresponding to a phase lag difference $\delta\Phi = 2\pi$; this phenomenon is attributable to the excitation of standing waves between the plasma edge and the cut-offs. On the other hand, it is rather insensitive to the details of the density profile.

While mode mixing should not make reflectometry impossible in a RFP of sufficiently large size, it must be taken into account for a correct interpretation of the signal from the central part of the discharge. For this purpose, simulation with FELRFP can be useful. In addition, the code can complement ray tracing to investigate the contribution of the reflection layer and of the low density region to the measured phase shift.

In appendices A and B we present the calling sequences of the two codes, a commented list of their input variables, and a few notes on their CPU time and memory requirements. Examples of the output come with the discussions of Sections 2 and 3.

To facilitate the understanding of the results presented in the following, the dispersion diagram for a typical RFP configuration is shown in Fig. 3. As well known, the X-wave encounters first the $R = 0$ cut off, so that both the Upper Hybrid resonance $S = 0$ and the electron cyclotron resonance $f = f_{ce}$ are unaccessible from the outside; the first harmonic resonance $f = 2f_{ce}$ can be encountered near the plasma edge in the lower part of the frequency scan. Also, the cut off of the X-wave occurs always at densities lower than the $P = 0$ cut off of the O-wave [14].

2. Ray Tracing of the X and O waves in a RFP configuration.

The ray tracing code RAYRFP is similar in structure to those developed for Lower Hybrid waves and Ion Cyclotron waves [15] in tokamaks. The main differences are:

1) The plasma equilibrium has been modified to describe a RFP configuration, neglecting toroidal effects. The Bessel Function Model is the default option, but different magnetic field profiles can be specified by the user.

2) The ray equations are obtained from the cold plasma dispersion relation for waves in the electron frequency range, and simplified according to the requirements of the present problem. In particular, the expansion in toroidal modes, necessary at lower frequency but superfluous in this case, has been suppressed, and replaced by the possibility of varying the initial incidence angle of the ray in both the poloidal and toroidal directions.

3) For the present problem, there is no need to integrate the power balance equation, as absorption is likely to be negligible under the experimental conditions. This equation has therefore been suppressed from the code for the sake of faster execution.

The cold plasma dispersion relation for waves in the electron frequency domain [14] is conveniently written:

$$H(\vec{r},\vec{k}) = Sn_\perp^4 + (P+S)n_\perp^2 n_\parallel^2 + Pn_\parallel^4 - (RL+PS)n_\perp^2 - 2PSn_\parallel^2 + PRL = 0 \qquad (1)$$

where $\vec{n} = \vec{k}c/\omega$; parallel and perpendicular refer as usual to the direction of the static magnetic field. The elements of the cold plasma dielectric tensor are:

$$R = 1 - \frac{X_e}{1-h_e} \qquad L = 1 - \frac{X_e}{1+h_e}$$

$$S = \frac{R+L}{2} \qquad P = 1 - X_e \qquad (2)$$

where

$$X_e = \frac{\omega_{pe}^2}{\omega^2} = 8.064 \cdot 10^{-11}\frac{n_e}{f^2} \qquad h_e = \frac{\Omega_{ce}}{\omega} = 28\frac{B}{f} \qquad (3)$$

(n_e in cm^{-3}, B in Tesla, f in Ghz.). The ray equations, in cylindrical coordinates r, ϑ, ς, with ς-axis along the RFP magnetic axis,

$$\begin{aligned}
\frac{dr}{d\tau} &= \frac{\partial H}{\partial k_r} \qquad \frac{dk_r}{d\tau} = -\frac{\partial H}{\partial r} \\
\frac{d\vartheta}{d\tau} &= \frac{\partial H}{\partial k_\vartheta} \qquad \frac{dk_\vartheta}{d\tau} = -\frac{\partial H}{\partial \vartheta} = 0 \\
\frac{d\varsigma}{d\tau} &= \frac{\partial H}{\partial k_\varsigma} \qquad \frac{dk_\varsigma}{d\tau} = -\frac{\partial H}{\partial \varsigma} = 0
\end{aligned} \qquad (4)$$

are easily obtained by implicit derivation of Eq. (1), taking into account that:

$$k_\perp^2 = k_r^2 + k_\eta^2$$

$$k_\eta = \frac{m}{r}\cos\Theta - k_\varsigma \sin\Theta \qquad (5)$$

$$k_\parallel = \frac{m}{r}\sin\Theta + k_\varsigma \cos\Theta$$

$$\cos\Theta = \frac{B_\varsigma}{\sqrt{B_\varsigma^2 + B_\vartheta^2}} \qquad \sin\Theta = \frac{B_\vartheta}{\sqrt{B_\varsigma^2 + B_\vartheta^2}}$$

Thus:

$$\begin{aligned}
\frac{\partial H}{\partial k_r} &= 2k_r \frac{\partial H}{\partial k_\perp^2} \\
\frac{\partial H}{\partial m} &= \frac{2}{r}\Big(\frac{\partial H}{\partial k_\perp^2} k_\eta \cos\Theta + \frac{\partial H}{\partial k_\parallel^2} k_\parallel \sin\Theta\Big) \\
\frac{\partial H}{\partial k_\varsigma} &= -2\Big(\frac{\partial H}{\partial k_\perp^2} k_\eta \sin\Theta - \frac{\partial H}{\partial k_\parallel^2} k_\parallel \cos\Theta\Big) \\
\frac{\partial H}{\partial r} &= \Big(X_e \frac{\partial H}{\partial X_e}\Big)\frac{1}{n_e}\frac{dn_e}{dr} + \Big(h_e \frac{\partial H}{\partial h_e}\Big)\frac{1}{B}\frac{dB}{dr} \\
&\quad - 2\Big\{\frac{m}{r^2}\Big(\frac{\partial H}{\partial k_\perp^2} k_\eta \cos\Theta + \frac{\partial H}{\partial k_\parallel^2} k_\parallel \sin\Theta\Big) + k_\eta k_\parallel \Big(\frac{\partial H}{\partial k_\perp^2} - \frac{\partial H}{\partial k_\parallel^2}\Big)\frac{d\Theta}{dr}\Big\}
\end{aligned} \tag{6}$$

About these equations, we can make the following comments:

- the numerical importance of the two terms proportional to dB/dr and $d\Theta/dr$ respectively allows neglecting toroidal curvature effects in the RFP case, as opposed to the Tokamak case;

- as a consequence, to this approximation, both the poloidal and the toroidal wavenumbers, m and k_ς, are conserved during propagation, so that the wave problem is effectively one-dimensional. This is a typical example of the great advantages offered by ray tracing even in cases where the full wave problem could be solved by integrating ordinary differential equations only.

The code RAYRFP can solve the ray equations in the form (4), or it can make use of the phase σ along rays as independent variable. For this purpose, Eqs. (4) are divided throughout by

$$\frac{d\sigma}{d\tau} = k_r \frac{\partial H}{\partial k_r} + m \frac{\partial H}{\partial m} + k_\varsigma \frac{\partial H}{\partial k_\varsigma} \tag{7}$$

This is particularly useful for the implementation of plots of the wavefronts. It can be shown that the rhs of (7) never vanishes at frequencies higher than the cut-off frequency of the ordinary mode.

The initial conditions are imposed on the outer magnetic surface, by specifying the initial ray direction, and wether the ordinary or the extraordinary wave is launched.

Some care is called for in dealing with the wave polarisation. Thus for example to launch a pure mode to begin with, the antenna has to be properly oriented with respect to the static magnetic field at the plasma edge. Ray tracing can then be used to investigate the

polarisation to be expected at the receiver position, particularly when this is situated at a non negligible angle with respect to the launching point. The wave polarisation is most easily expressed at each point in a local reference frame (x, y, z) with z-axis along $\vec{B}_o$. From Maxwell equations in the Eikonal approximation one easily obtains in this frame:

$$E_x : E_y : E_z = -n_{\|} D(P+Q) \quad : \quad i n_{\|} Q \quad : \quad n_{\perp} D \tag{8}$$

where

$$Q = \sqrt{B'^2 + 4 n_{\|} P D^2} - B' \qquad B' = RL - PS + n_{\|}^2 (P - S)$$

$$D = (R - L)/2$$

This form of the polarisation equations, although not the simplest possible, has been chosen because it remains meaningful also in the case of the O-wave with $n_{\|} = 0$. From the knowledge of E_x, E_y, E_z the components of $\vec{E}$ in the laboratory frame are easily worked out.

Fig. 4 a shows an example of the field pattern in the poloidal cross-section for typical RFX conditions ($a = 40$ cm, $B_0 = 2.2$ tesla, $n_e(0) = 1.4 \cdot 10^{14}$ cm^{-3}). The frequency is 100 Ghz, with launcing in the ordinary mode. The diameter of the antenna is taken to be 9 cm and the angular spread $\pm 4^o$ (about twice the theoretical optimum at this frequency). Both effects mentioned in the introduction, namely the angular spreading of the radiation pattern following reflection, and the deviation of the reflection caustic from a constant density surface, are clearly visible (a similar spread takes place also in the toroidal direction, fig. 4 b). It is therefore important for the receiving antenna to be as close as possible to the emitting one; even better would be to use the same horn for both purposes.

Fig. 5 illustrates the use of the RAYRFP code to simulate a complete reflectometry scan. With respect to the direct solution of the phase lag equation, this procedure has the disadvantage that the interpretation of the measurements requires a trial and error modification of the density profile assumed in the code. It can nevertheless be useful, particularly in the case of X-mode reflectometry.

Finally, Fig. 6 is an example of extraordinary wave launching, under conditions otherwise identic to those of Fig. 4, except that the frequency was chosen 120 Ghz to compensate for the fact that at any given frequency the cut off of the X-mode is located at lower density than the one of the O-mode. It also appears that refraction is somewhat more important for this polarisation than for the previous one.

3. Mode mixing in the RFP configuration.

Ray tracing is based on the assumption that the X and O modes of the uniform plasma propagate independently from each other also in the real, inhomogeneous configuration. Because of the large shear of the RFP, however, this assumption can be legitimately questioned. Even in a relatively large device such as RFX, the relative variation of $\tan\Theta = B_\theta/B_\phi$ over one wavelength amounts to a few percent at $f = 100$ Ghz. Because of the great length of the optical path (about 100 wavelengths in the example of Fig. 4), the cumulative effect of coupling between modes will not be negligibly small. At lower frequencies the optical length is smaller, but the relative variation of the shear parameter correspondingly larger.

Although mode mixing could be used in principle to measure *simultaneously* the density and the magnetic field profiles, it clearly makes the analysis of the experimental signal more complicated, and actually hardly possible without a much more detailed theoretical analysis than offered by ray tracing. Fortunately, a full wave analysis is possible in the case of the RFP, since toroidal effects can be neglected, and only para-equatorial waves with $m_\theta \simeq n_\phi \simeq 0$ need to be considered (the second circumstance greatly simplifies the equations to be solved, but is not as essential as the first one). For such waves, Maxwell equations can be written

$$\begin{aligned}
&\frac{d}{dr}\left(\frac{1}{r}\frac{d}{dr}(rE_\theta)\right) + \frac{\omega^2}{c^2}\left\{\left(P\sin^2\Theta + \frac{RL}{S}\cos^2\Theta\right)E_\theta + \left(P - \frac{RL}{S}\right)\cos\Theta\sin\Theta E_\phi\right\} = 0 \\
&\frac{1}{r}\frac{d}{dr}\left(r\frac{dE_\phi}{dr}\right) + \frac{\omega^2}{c^2}\left\{\left(P - \frac{RL}{S}\right)\cos\Theta\sin\Theta E_\theta + \left(P\cos^2\Theta + \frac{RL}{S}\sin^2\Theta\right)E_\phi\right\} = 0
\end{aligned} \tag{9}$$

For $\Theta = 0$ and $\Theta = \pi/2$ these two equations decouple into one for the ordinary and one for the extraordinary wave, respectively; the same result is obtained by an appropriate rotation if Θ is arbitrary but constant, E_θ and E_ϕ being related to the X and O wave components by

$$E_X = E_\theta\cos\Theta - E_\phi\sin\Theta \qquad E_O = E_\theta\sin\Theta + E_\phi\cos\Theta \tag{10}$$

When Θ is a function of radius, therefore, coupling between the two modes is unavoidable. If E_X and E_O are used as variables instead of E_θ and E_ϕ, Eqs. (9) become the cylindrical equivalent of Fösterling coupled equations [16]. In the general case, they can be solved only numerically. It is nevertheless worth mentioning that their slab equivalent with constant shear ($d\Theta/dx = const.$) has been investigated in some details by M. A. Heald [13]; also, Fidone and Granata [17] have treated perturbatively the case of weak shear.

Runge-Kutta integration tends to pick up the wrong solution in the regions where one or both waves are evanescent. To avoid this problem, we have used instead a recently developed general purpose Finite Element subroutine, employing cubic Hermite interpolating functions on each element, which has already proved useful in other wave problems of similar structure [18]. Details of the numerical method can be found elsewhere [19]; here it will be sufficient to mention that cubic Hermite interpolation, ensuring the continuity of the fuctions and their derivatives at each mesh point, guarantees excellent convergence rates, making this method competitive with more conventional ones also from the point of view of execution speed and accuracy.

For the complete formulation of the problem, we have also to specify the boundary conditions. Those at the plasma centre are obvious (in practice, they are imposed not at the plasma centre, but a few evanescent lengths to the inside of the innermost cut-off). At the plasma boundary we assume that the polarisation of the incident wave is selected by the orientation of the antenna, while the complex amplitude of the reflected waves are left free. In other words, for $r \geq a$ we assume:

$$\begin{aligned} E_\theta &= \frac{\rho_\theta H_1^1(k_o r) + \delta_\theta H_1^{(2)}(k_o a)}{H_1^{(2)}(k_o r)} \\ E_\phi &= \frac{\rho_\phi H_o^1(k_o r) + \delta_\phi H_o^{(2)}(k_o r)}{H_o^{(2)}(k_o a)} \end{aligned} \tag{11}$$

where H_n^α are Hankel functions, and $k_o = \omega/c$. δ_θ and δ_ϕ are chosen according to the antenna polarisation, while ρ_θ and ρ_ϕ are determined by imposing continuity of the solution and its derivatives at the plasma boundary. Note that energy conservation requires

$$\rho_\theta^2 + \rho_\phi^2 = \delta_\theta^2 + \delta_\phi^2 \tag{12}$$

This condition cannot be enforced separately upon the code, and therefore provides an independent check of the accuracy of the numerical solution. In the following examples, with 10 to 20 mesh steps per (vacuum) wavelength, it was satisfied to 10^{-6} or better.

It should also be mentioned that the real pattern of the antenna contains of corse also components with non-zero poloidal and toroidal wavenumbers, as it is obvious from the fact that it is localised in both θ and ϕ. Thus the results from our code overestimate the amplitude of the reflected waves with respect that of the launched wave. This is however of little relevance, due to the way in which the measurements are made, as discussed at the end of this section. What is important is the resulting polarisation of the reflected wave, which should be accurately given by FELRFP. Extension of the code to superpose several Fourier components would not be difficult if required.

Figs. 7 a) and b) show the O and X-waves pattern at a frequency $f = 75$ Ghz, with O-wave launching; Figs. 8 a) and b) show the same case with X-wave launching (note that both the horizontal and vertical scales vary from one plot to the other; all amplitudes are normalized so that the amplitude of the launched wave is unity). The mixing parameter μ, defined as the modulus squared of the reflection coefficient of the wave *which is not launched*, is for this case $5.5 \cdot 10^{-2}$; it does not depend on the orientations of the antenna, illustrating the unitary nature of the scattering matrix associated with equations (11).

A frequency scan reveals that μ is not a monotonic function: on the contrary, it is deeply modulated, with minima equal to zero, separated by the frequency interval corresponding to the increase of the optical path length by one wavelength. As the frequency increases, the maxima of μ increase and their spacing decreases, as it is seen by comparing Figs. 9 and 10. These figures show μ versus frequency in the intervals between 70 and 78 Ghz and between 90 and 98 Ghz respectively. The cause of this behaviour must be the excitation of standing waves between the cut-offs and the plasma boundary. The modulation is not sinusoidal, probably reflecting the asymmetry of the virtual cavity due to the density and magnetic field gradients. This inhomogeneity becomes less and less important as the frequency increases and the WKB approximation holds over a larger and larger fraction of the optical path: this is clearly reflected in the form of $\mu(f)$. Figs. 11 a) and b) show the wave patterns at 90.0 and 90.5 Ghz, respectively near a maximum and near the next minimum of the mixing parameter (in both cases with O-launching). The amplitude of the X-mode inside the plasma is not essentially different in the two cases; its envelope however shows a long wavelength modulation such that a maximum in amplitude occurs near $r = a$ in the first case, a minimum in the second.

Fig. 9 b) illustrates the increase of the mixing parameter with decreasing plasma dimensions, by comparing the RFX results with those for a RFP with the same density and magnetic field profiles but with minor radius $a = 20$ cm. The frequency separation between successive peaks of μ is doubled, as expected; in addition, the peak values are about twice as large, showing that the decrease in length of the optical path does not compensate the increase in the shear variation per wavelength.

The excitation of standing waves suggests a considerable mismatching between the vacuum wave and the waves in the plasma. Indeed, the WKB approximation is poor near the plasma edge. To see how sensitive the results are to the assumed density profiles there, we have compared a discontinuous profile with $n(a) = 0.1 \cdot n(0)$, (Fig. 9 a, solid curve), and an almost continuous profile with a scrape off layer extending from $r = 40$ to $r = 45$ cm, with density decreasing exponentially with decay length $= 2$ cm;

the boundary conditions are imposed in this case at $r = 45$ cm (Fig. 9, dotted curve). The smoother profile suppresses some of the structure near the peaks of the mixing parameters; the results are nevertheless quite insensitive to the details of the density profile near the plasma boundary. This suggests that mixing is indeed due to shear, and not to mismatching. This conclusion is also supported by the fact that mixing increases with frequency, while the importance of the density gradient near the edge should decrease as the wavelength becomes shorter.

To check that the observed mode mixing is indeed due to shear, we have built in the code the possibility of simulating a straight tokamak equilibrium, with $B_\phi = const.$ and

$$B_\theta = \frac{\mu_o}{r} \int_o^r r J_\phi(r) dr \tag{13}$$

where J_ϕ is the current density. Assuming a safety factor $q = aB_\phi/RB_\theta = 3$, a parabolic current profile, and all other parameters as in the RFX case, we find that in the frequency range between 90 and 100 Ghz the mixing coefficient in the low-shear tokamak configuration remains lower than 10^{-3}, while showing the same kind of modulation as in the RFP case. For comparison, the X-wave component excited by mode mixing in this case at 90 Ghz is shown in Fig. 12.

To understand the consequences of the above results for the practical implementation of reflectometry in a RFP device, we first note that the O and X modes retain their identity throghout the plasma, so that for example Eq. (2) can still be applied with excellent accuracy. Also, the unwanted X-wave is easily rejected by exploiting the fact that a rectangular waveguide is a very good polarizing filter: both the emitter and the receiver antennas should be oriented with their small sides parallel to the magnetic field at the plasma edge. The question is therefore wether the phase shift $\Phi(f)$ of the O-mode alone can be measured in spite of mode mixing. At least in the RFX case this seems to be feasible without difficulty.

The phase shift $\Phi(f)$ is measured in practice by mixing a reference signal from the launched wave with one from the reflected wave, and measuring the frequency interval between successive minima of the resulting signal (near 90 Ghz, two such minima are separated by about 0.39 Ghz in the case of Fig. 10). If all the power would remain in the O-wave (and neglecting the frequency variation of the response of the various circuit elements), an appropriate choice of the amplitude of the two signals to be mixed would produce a perfectly regular succession of maxima and minima. Mode mixing however modulates the amplitude of the reflected wave with the O-polarisation, so that the situation looks as in Figs. 13 and 14 a: the compound signal will also be modulated.

Although the peak value of μ is around 0.2 in the frequency range chosen, the correct identification of minima should nevertheless be easy.

In principle, it is also possible to mix the signal from the launched wave with the one from the reflected wave in the X polarisation (received by a waveguide oriented perpendicularly to the emitter). As shown in Figs. 13 and 14 b, this gives a much more irregular compound pattern. A careful analysis of this signal could give some information on the magnetic field in the plasma (a similar procedure has been attempted by Cano et al. [20], inverting the role of the X and O waves; it is not to be confused with the method proposed by De Marco and Segre [21], which relies on mode "splitting" due to the plasma birifrangence, assuming no mode mixing). However this method would work poorly at low frequencies, where mode mixing is very small (also, at these frequencies, the X wave could be attenuated by transiting through the first electron cyclotron harmonic resonance, which is not taken into account in the code). As a consequence, the most interesting external layer in which deviations from the BFM are expected could hardly be explored in this way.

4. Conclusions.

We have presented two codes for the numerical simulation of reflectometry in Reversed Field Pinches, and illustrated their usefulness with a few examples; additional applications are easily imagined. In particular, our results predict a non negligible mixing between the two cold plasma waves due to the shear of the static magnetic field, as soon as the relative variation of $\vec{B}$ per wavelength is large, or when its effect accumulates over a large number of wavelengths. The second case occurs for frequencies probing the plasma core even in relatively large devices. This should not rule out the application of reflectometry to reverse field pinches, however, provided that the direction of the static magnetic field near the plasma edge is known with sufficient accuracy, so that the unwanted cold plasma mode (usually the X-wave) can be filtered away both in emission and in reception.

Appendix A: The Ray Tracing code RAYRFP.

The ray-tracing code RAYRFP can be called from any "user "program, with the statement

CALL RAYRFP

The user program must contain the following two labelled COMMON blocks

COMMON /CINOUT/ RPLASM, DENC, AMU, BZERO, FREQCY, AWIDTH, ANGLTH, ANGLPH

COMMON /CONTRL/ DPRINT, DANGTH, DANGPH, NANGTH, NANGPH, IWAVE, INDVAR, IPRINT, IGRAPH, IPLPRO

and must initialise their variables before calling RAYRFP. The meaning of these variables is as follows.

RPLASM	(real)	plasma radius, in cm.
DENC	(real)	central density, in cm.
AMU	(real)	pinch parameter ($= 2\vartheta$).
BZERO	(real)	central magnetic field, in Tesla.
FREQCY	(real)	frequency, in Ghz.
AWIDTH	(real)	half-width of the antenna, in cm.
ANGLTH	(real)	inclination of the central ray in the poloidal cross-section (degs).
ANGLPH	(real)	inclination of the central ray in the toroidal cross-section (degs).
DPRINT	(real)	interval between wavefronts (wavelengts).
DANGTH	(real)	increment of the ray inclination in the poloidal cross-section (degs).
DANGPH	(real)	increment of the ray inclination in the toroidal cross-section (degs).
NANGTH	(integ.)	number of rays in the poloidal cross-section.
NANGPH	(integ.)	number of rays in the toroidal cross-section.
IWAVE	(integ.)	emitter antenna orientation: IWAVE, = 1 Extraordinary wave; IWAVE, = -1 Ordinary wave.
INDVAR	(integ.)	choice of the independent variable (†): INDVAR = 1, phase as independent variable; INDVAR = 0, τ as independent variable.

IPRINT (integ.) printed output:
IPRINT = 1, details printed every DPRINT wavelengths;
IPRINT = 0, only the starting data printed for each ray.

IGRAPH (integ.) graphical ouptut:
IGRAPH = 1, the plots are executed;
IGRAPH = -1, the plots are skipped.

IPLPRO (integ.) plotting $n_e(r)$ and $\vec{B}(r)$:
IPLPRO = 1, the profiles are plotted;
IPLPRO = -1, the profiles are skipped.

(†) When the phase is chosen as independent variable, a ray propagating perpendicularly to the magnetic surfaces (radially inward) cannot be followed after reflection. If plot are desired, the choiche INDVAR = 1 is to be preferred, but the ray with ANGLTH = 0. and ANGLPH = 0. should be avoided.

In addition, the user code must provide the function PRONE(X) = $n_e(r/a)$ which evaluates the radial density profile (it can be normalised arbitrarily; it is renormalised by the code so that $n_e(0)$ = DENC).

In the standard version, no more than 11 rays with 200 wavefronts can be plotted in a single run. Although this should be sufficient in most cases, it is possible to enlarge the DIMENSIONs of the arrays for the graphical output by altering the values of the PARAMETERs NGR (number of rays) and IEQMAX (number of wavefronts) before the COMMONs in each subroutine.

RAYRFP can be used in two different modes. At a fixed frequency one can plot the field pattern, as in Figs. 4. On a CRAY-1, a typical run with 10 rays and 40-50 wavefronts executes in 10 to 12 sec, a substantial fraction of this time being devoted to the execution of the plots. Alternatively, one can make a frequency scan by letting ANGLTH = 0, ANGLPH = 0, NANGTH = 1, NANGPH = 1, INDVAR = 0, IGRAPH = 0, (usually also IPRINT = 0), and by putting the call to RAYRFP within a loop incrementing FREQCY. In this way a scan like the one of Fig. 5 can be obtained in 4 to 6 sec only, depending on the frequency step used (all these times include compilation).

Appendix B: The Finite Element code FELRFP.

The finite element code FELRFP can be called from any "user "program, with the statement

CALL FELRFP

The user program must contain the following labelled COMMON:

COMMON /CINOUT/ RPLASM, RTORUS, DENC, AMU, BZERO, FREQCY, AQU, DFREQ, WSCRAP, GLDN, NSTEP, IWAVE, IPRINT, IGRAPH, NFREQ, IEQUIL

and must initialise their variables before calling RAYRFP. The meaning of these variables is as follows.

RPLASM	(real)	plasma radius, in cm.
RTORUS	(real)	torus radius (†)
DENC	(real)	central density, in cm.
AMU	(real)	pinch parameter ($= 2\vartheta$).
BZERO	(real)	central magnetic field, in Tesla.
FREQCY	(real)	frequency, in Ghz.
AQU	(real)	safety factor q(a) (†)
DFREQ	(real)	step of FREQCY.
WSCRAP	(real)	width of the scrape-off layer (cm).
GLDN	(real)	decay length of the density in the scrape-off layer (cm).
NSTEP	(integ.)	number of mesh elements per vacuum wavelength.
IWAVE	(integ.)	emitter antenna orientation:
		IWAVE, = 1 Extraordinary wave;
		IWAVE, = -1 Ordinary wave.
IPRINT	(integ.)	printed output:
		IPRINT = 1, details printed for all mesh points;
		IPRINT = 0, only the reflection coefficient printed.
IGRAPH	(integ.)	graphical ouptut:
		IGRAPH = 1, the plots are executed;
		IGRAPH = -1, the plots are skipped.
NFREQ	(integ.)	number of frequency values in a scan.
IEQUIL	(integ.)	discharge configuration chosen:
		IEQUIL = 1, Reversed Field Pinch;

IEQUIL = 0, Straight Tokamak.

(the variables with a (†) are ignored when IEQUIL = 0)

The maximal DIMENSIONs of the mesh arrays allow 2000 elements, which means that if d is the distance between the plasma edge and the most internal cut off, df/c should not exceed (2000/NSTEP). If this condition is not satisfied, the code issues the message

"It was impossible to establish a mesh "

and stops. To cure this failure, one can reduce NSTEP, or, if this is not desirable, one can increase the value of the PARAMETER NPTMAX in all the subroutines in which it appears.

In addition, the user code must provide the function PRONE(X) = $n_e(r/a)$ which evaluates the radial density profile (it can be normalised arbitrarily; it is renormalised by the code so that $n_e(0)$ = DENC).

The CPU time required to run FELRFP depends of course on the number of wavelengths between the plasma edge and the most internal cut-off, and on wether or not the field pattern are plotted. A run with plots, for a frequency such that $f = f_{pe}$ 20 cm from the edge, requires 8 to 10 sec, mostly because of the graphical output (it should be noted that for a good visual result, NSTEP shold be 15 to 20 when plots are made; for accuracy sake only, NSTEP = 5 to 10 would suffice). A frequency scan such as the one leading to fig. 10 (NFREQ = 80, no plots, penetration length of the order of 20 cm, or about 50 wavelenths, i.e. 500 elements) requires 30 to 40 sec.

References

1 K. C. Budden, Radio waves in the ionosphere, Cambridge Univ. Press (Cambridge 1961).

2 V.L. Ginzburg, Propagation of electromagnetic waves in plasma, Gordon and Breach (New York 1961).

3 A.I. Anisimov et al., Sov. Phys. Tech. Phys. **5** (1961) 939.

4 Equipe TFR, Nucl. Fusion **18** (1978) 647.

5 J.L. Doane, E. Mazzuccato, G.L. Schmidt, Rev. Sci. Instrum. **52** (1981) 12.

6 R. Cano, A. Cavallo, Report EUR-CEA-FC 1137, Fontenay aux Roses (1981).

7 F. Simonet, Rev. Sci. Instrum. **56** (1985) 664.

8 Equipe TFR, Plasma Physics **27** (1985) 1255.

9 G. Itchenko, H. Botollier-Curtet, accepted for pubblication in Rev. Sci. Instrum., 1986.

10 G. Rostagni et al., Proc. Fusion Technology, 1984, Vol 1 p. 189, (CEC - Pergamon Press, 1984).

11 J. B. Taylor, Proc. V Int. Conf. on Plasma Physics and Contr. Nucl. Fusion Res., Vol 1 p, 161 (IAEA, Vienna, 1974).

12 S. Ortolani, Europhysics News **15** (1984) 5.

13 M. A. Heald, Plasma Physics **6** (1964) 617.

14 T.H. Stix, The theory of plasma waves, McGraw-Hill (New York, 1962).

15 M. Brambilla, Computer Physics Reports, **4** (1986) 71.

16 K. Fösterling, Hochfrequenztech. Elektroakust. **59** (1942) 10.

17 I. Fidone, G. Granata, Nucl. Fusion **11** (1971) 133.

18 M. Brambilla, T. J. Krucken, Proc XII Europ. Conf. on Contr. Fusion and Plasma Phys., Schliersee 1986, Vol 2, p. 89.

19 K. Appert et al., Computer Physics Comm., **40** (1986) 73.

20 R. Cano, M.J. Schwartz, B. Zanfagna, Phys. Fluids **15** (1972) 479.

21 F. De Marco, S. Segre, Plasma Phys. **14** (1972) 245.

Figure Captions.

Fig. 1 Working scheme of a reflectometry experiment.

Fig. 2 Radial profiles of the magnetic field components in a Reversed Field Pinch: experimental values (full lines) and Bessel Function Model (broken lines).

Fig. 3 Schematic dispersion diagram for the reversed field pinch in the frequency range suited for reflectometry.

Fig. 4 Ray tracing of the O-wave in the poloidal cross-section. Plasma parameters: $a = 40$ cm, Bessel Function model of the magnetic field with $\vartheta = 1.5$ and $B(0) = 2.2$ Tesla; parabolic density profile with $n_e(0) = 1.4 \cdot 10^{14}$ cm^{-3} and $n_e(a) = 1.4 \cdot 10^{13}$ cm^{-3}. Plotted wavefronts are spaced two wavelengths apart.

Fig. 5 Simulation of a frequency scan (O-mode launching): a) 40 cm $\leq r \leq$ 10 cm; b) central region.

Fig. 6 Ray tracing of the X-wave in the poloidal cross-section (same parameters as in Fig. 4).

Fig. 7 Electric field amplitude of the para-equatorial wave, plasma parameters as in Fig. 4, emitting antenna in the O-mode orientation: a) O-wave component; b) X-wave component.

Fig. 8 Electric field amplitude of the para-equatorial wave, antenna in the X-mode orientation: a) O-wave component; b) X-wave component.

Fig. 9 Mixing parameter in the range $70 \leq f \leq 78$ Ghz: a) plasma parameters as in Fig. 4 (full curve); with the addition od a 5 cm scrape-off layer (broken curve). b) $a = 20$ cm, other parameters as above.

Fig. 10 Mixing parameter in the range $90 \leq f \leq 98$ Ghz. Plasma parameters as in Fig. 4.

Fig. 11 Electric field distribution of the X component (antenna in the O-orientation). a) $f = 90$ Ghz, near a maximum of the mixing parameter. b) $f = 90.5$ Ghz, near a minimum of the mixing parameter.

Fig. 12 Extraordinary wave excited in the case of a straight Tokamak configuration ($q = 3$, other parameters as in the RFP of Fig. 4). Launched wave in the O polarisation with unit amplitude, $f = 90$ Ghz.

Fig. 13 Complex plane representation of the reflected waves between 90 and 91 Ghz, for the situation of Fig. 10.

Fig. 14 Superposition of the reflected waves of Fig. 14 with a reference signal from the launched wave (arbitrary units).

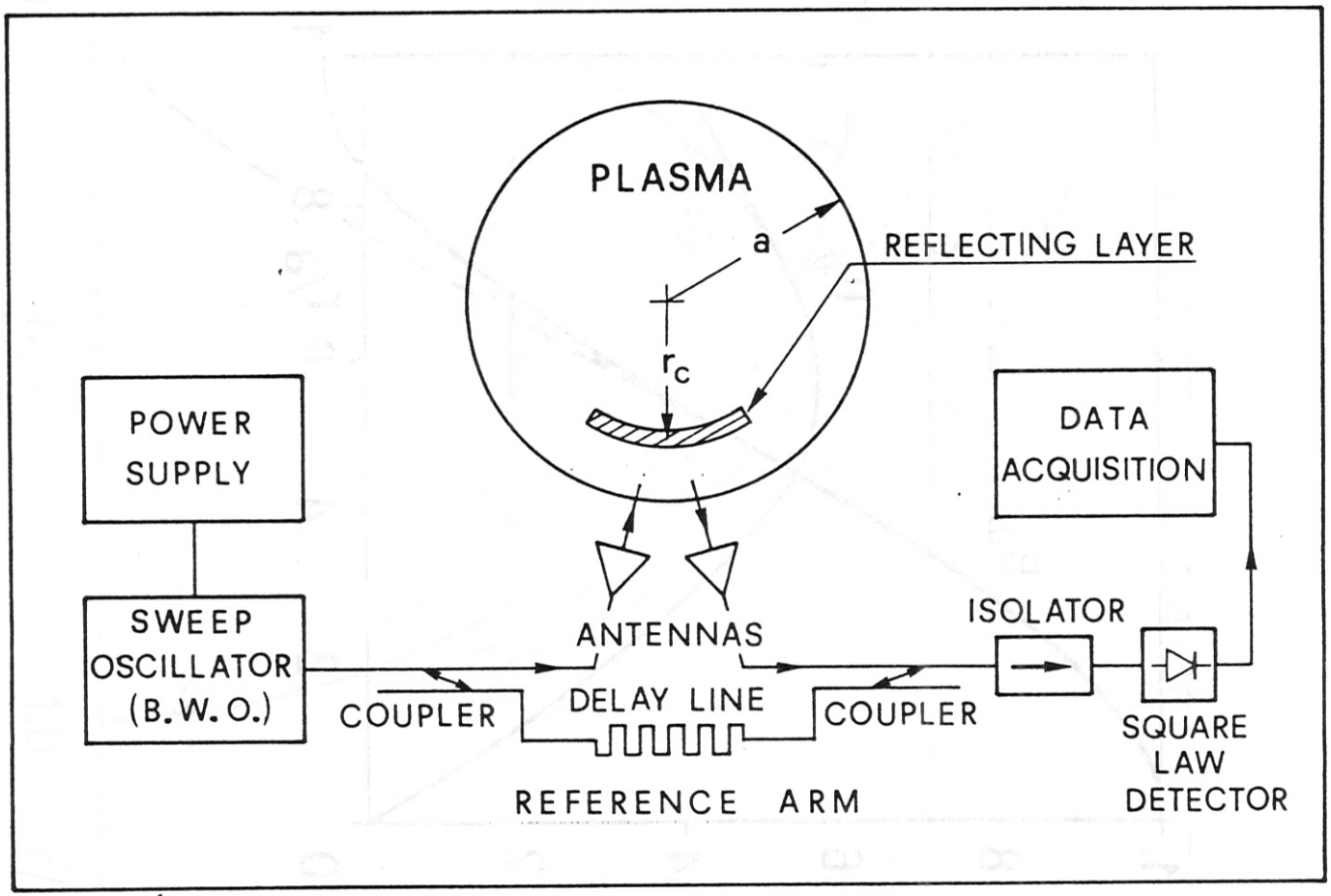
PLASMA
a
REFLECTING LAYER
r_c
POWER SUPPLY
DATA ACQUISITION
SWEEP OSCILLATOR (B.W.O.)
ANTENNAS
ISOLATOR
COUPLER
DELAY LINE
COUPLER
SQUARE LAW DETECTOR
REFERENCE ARM

Fig. 1

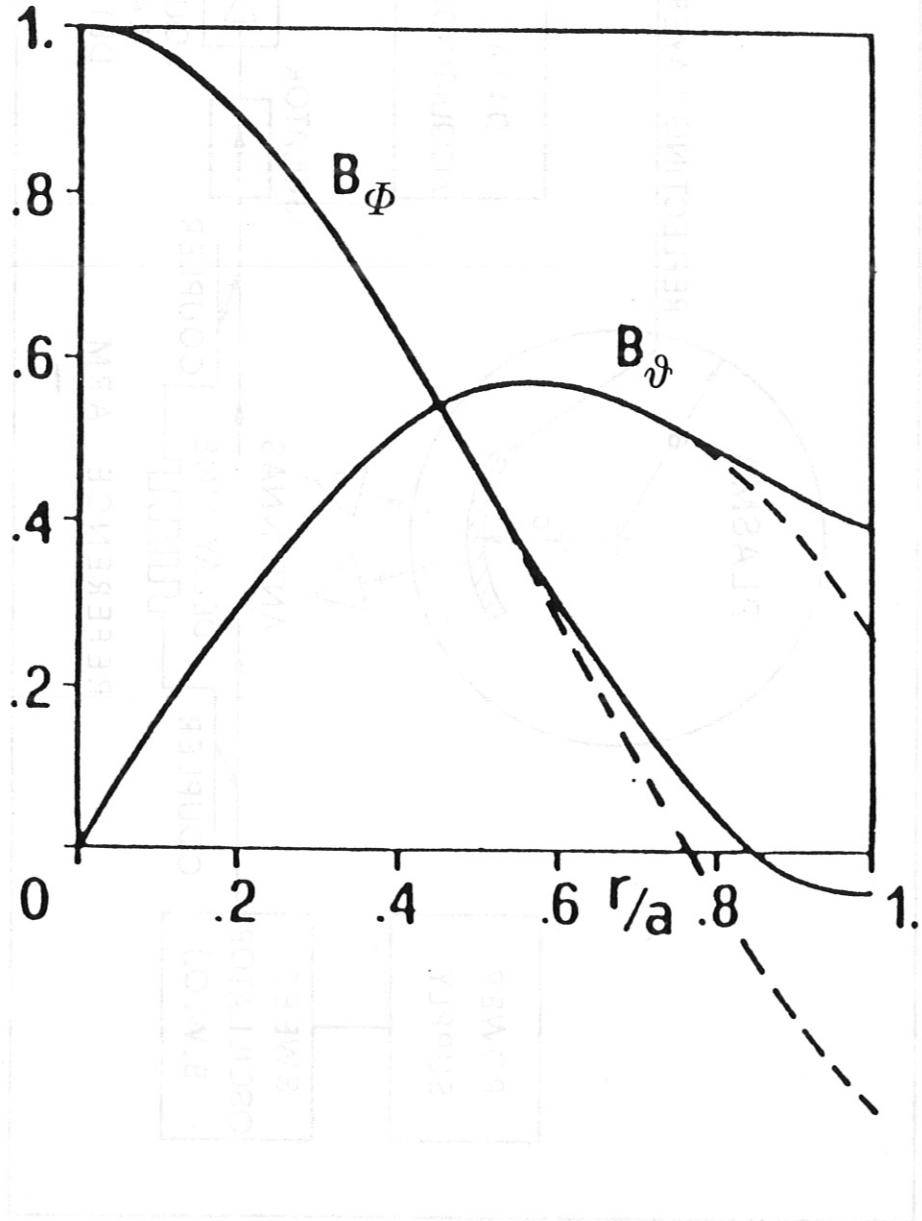

Fig. 2

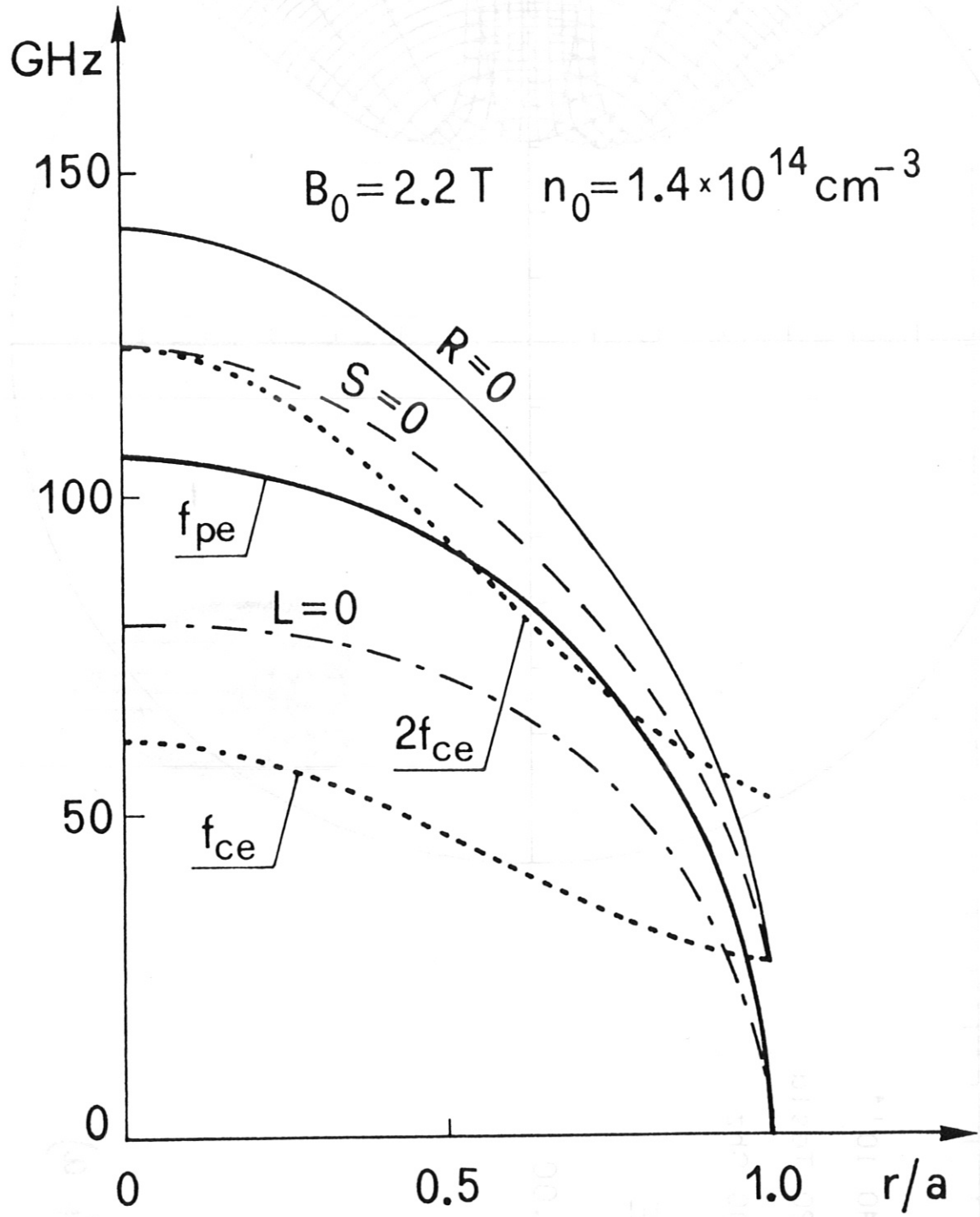
GHz
150
100
50
0
$B_0 = 2.2\ T$ $n_0 = 1.4 \times 10^{14}\ cm^{-3}$
R=0
S=0
f_{pe}
L=0
$2f_{ce}$
f_{ce}
0
0.5
1.0
r/a

Fig. 3

IPP-CRAY 07.86 08:27:56 MAB264 J2-03 001

N_0 = 1.40 10^{14}

B_0 = 2.20 Tesla

F = 100.00 Ghz

O-WAVE

ΔS = 2.00

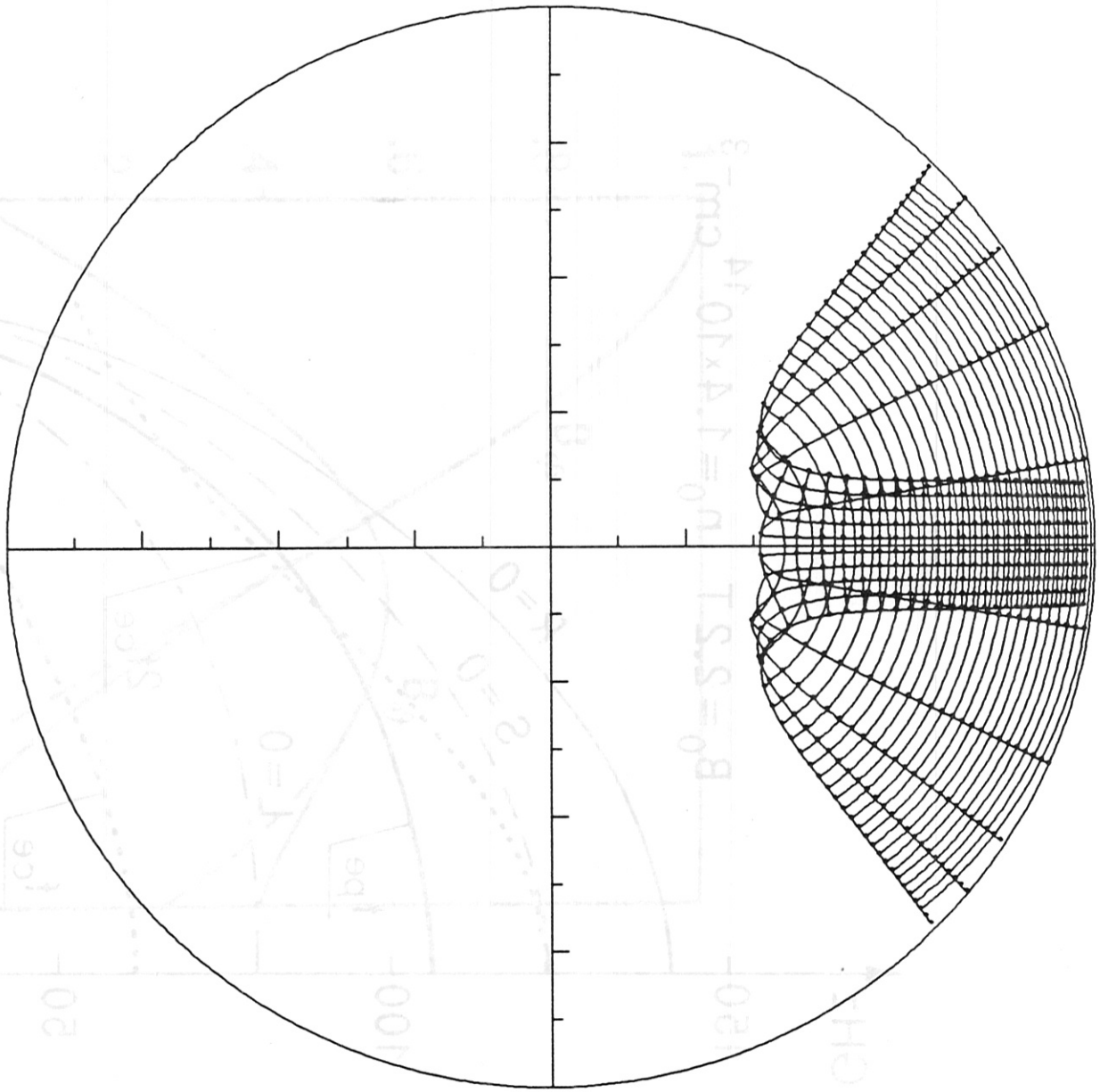

Fig 4 a)

IPP-CRAY 04.07.86 08:27:58 MAB264 J2-03 002

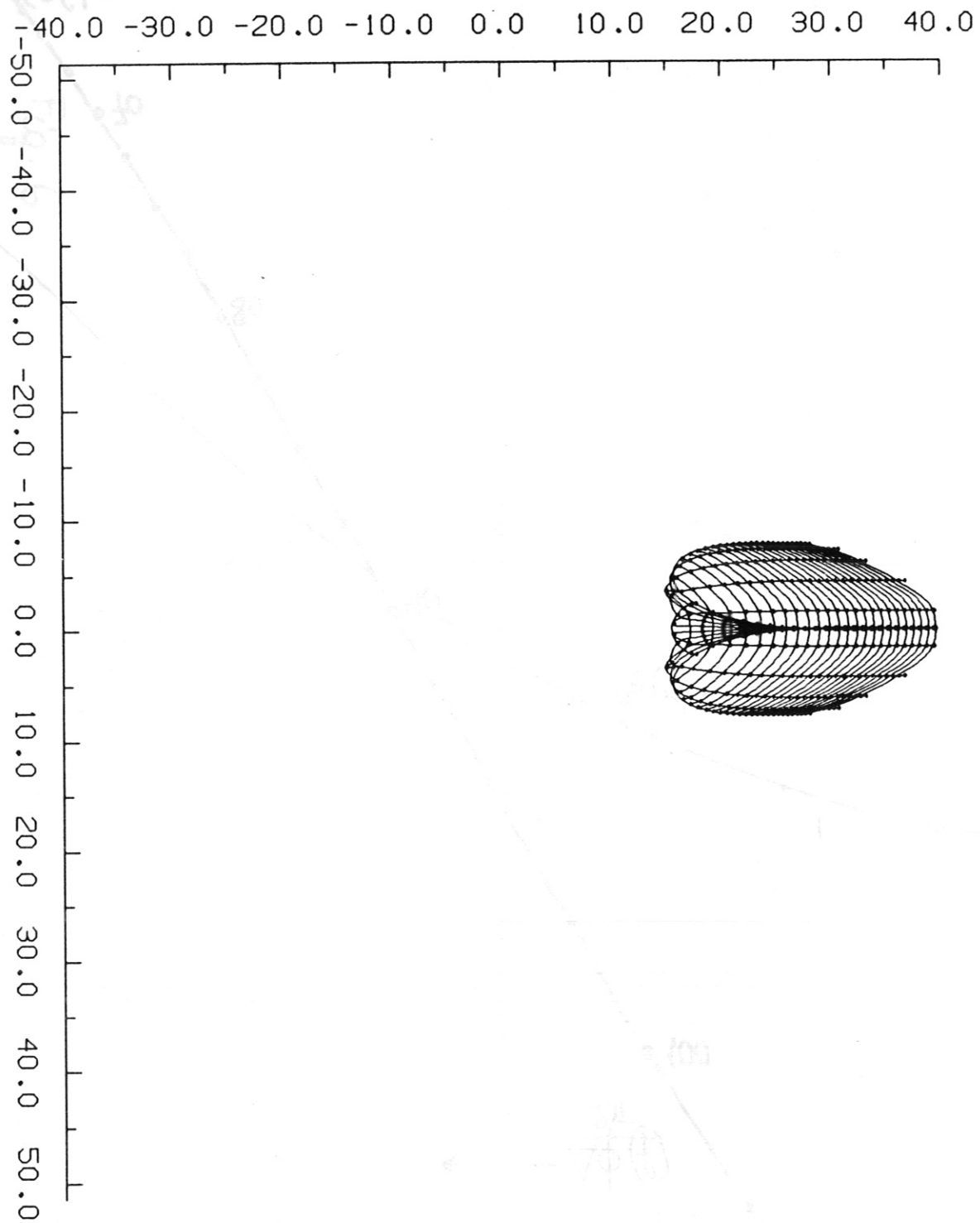

Fig. 4 b)

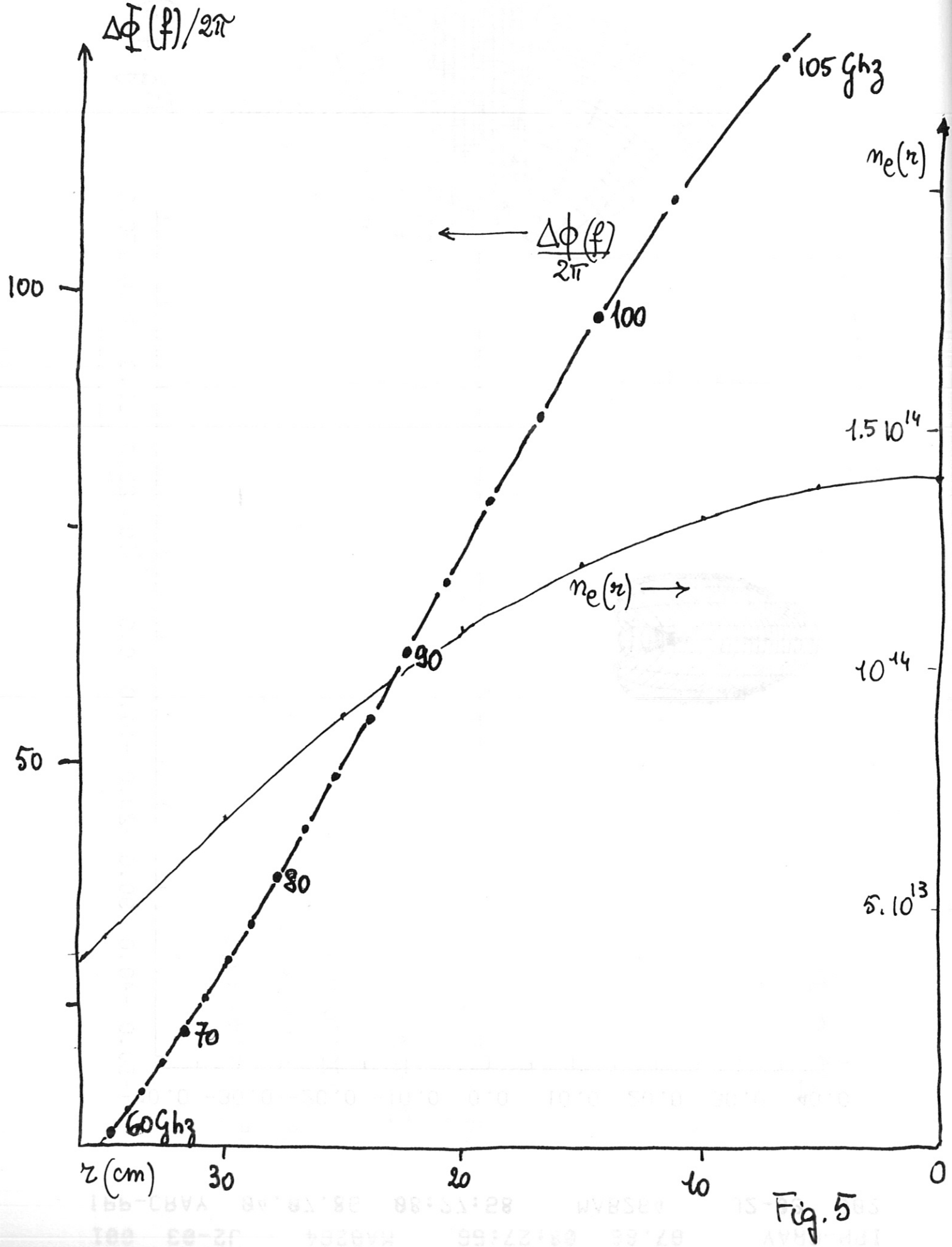
$\Delta\Phi(f)/2\pi$
105 Ghz
$n_e(r)$
$\leftarrow \frac{\Delta\phi(f)}{2\pi}$
100
100
$1.5\,10^{14}$
$n_e(r) \rightarrow$
90
10^{14}
50
80
5.10^{13}
70
60Ghz
r (cm)
30
20
10
0

Fig. 5

IPP-CRAY 07.86 11:56:19 MAB325 J2-03 001

N_0 = 1.40 10^{14}

B_0 = 2.20 Tesla

F = 120.00 Ghz

X-WAVE

ΔS = 2.00

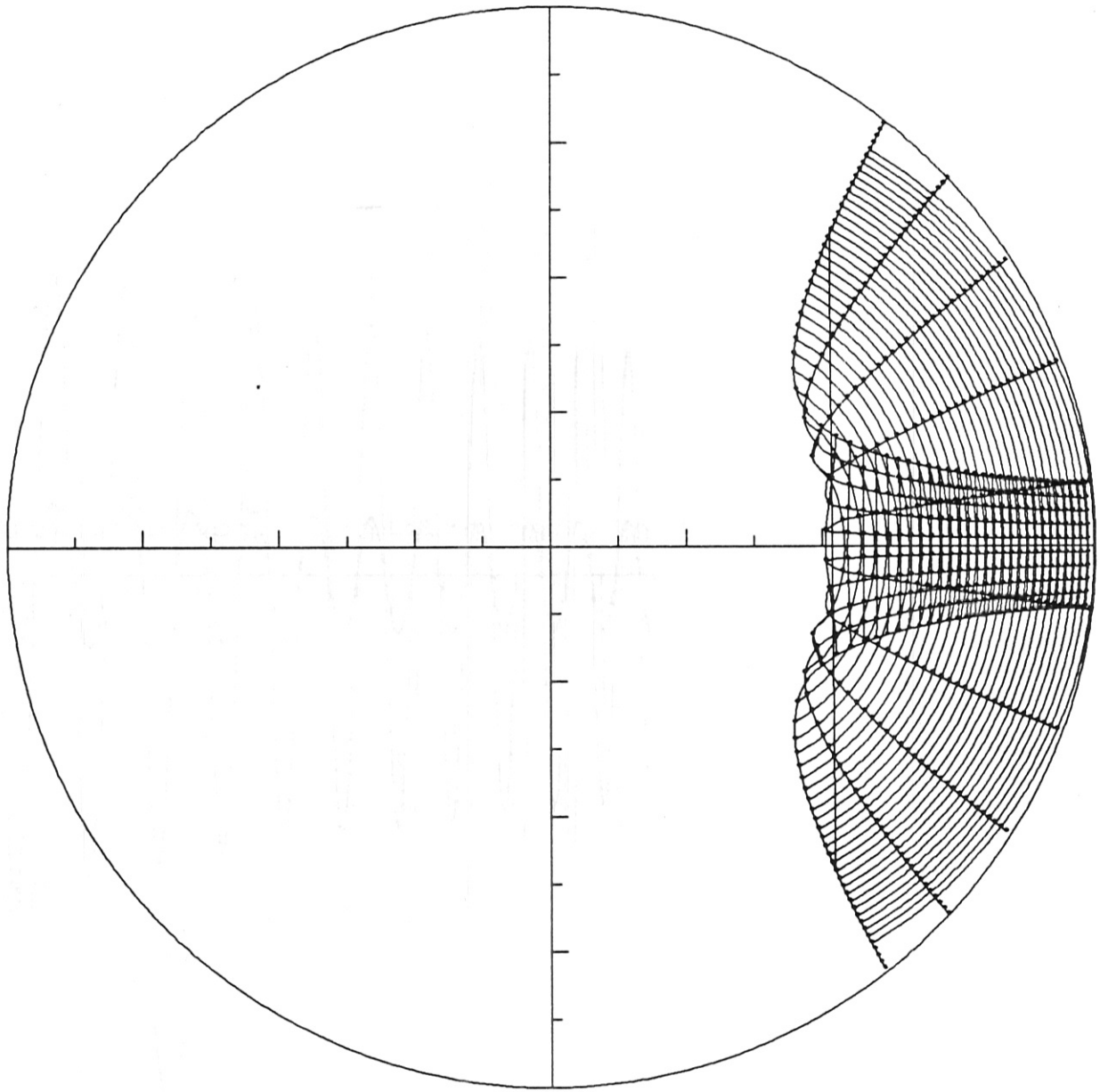

Fig. 6

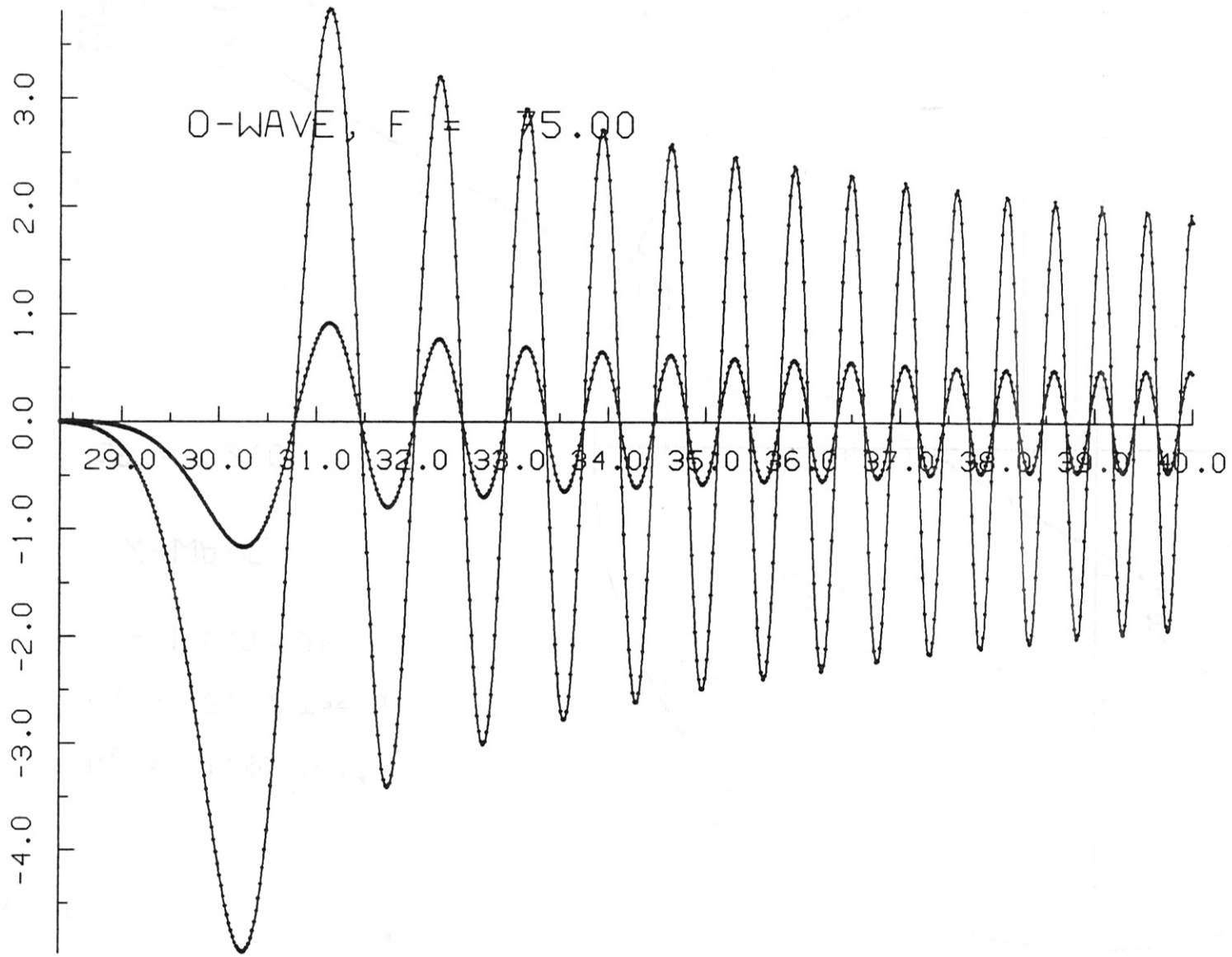
O-WAVE, F = 75.00
3.0
2.0
1.0
0.0
-1.0
-2.0
-3.0
-4.0
29.0
30.0
31.0
32.0
33.0
34.0
35.0
36.0
37.0
38.0
39.0
40.0

Fig. 7a

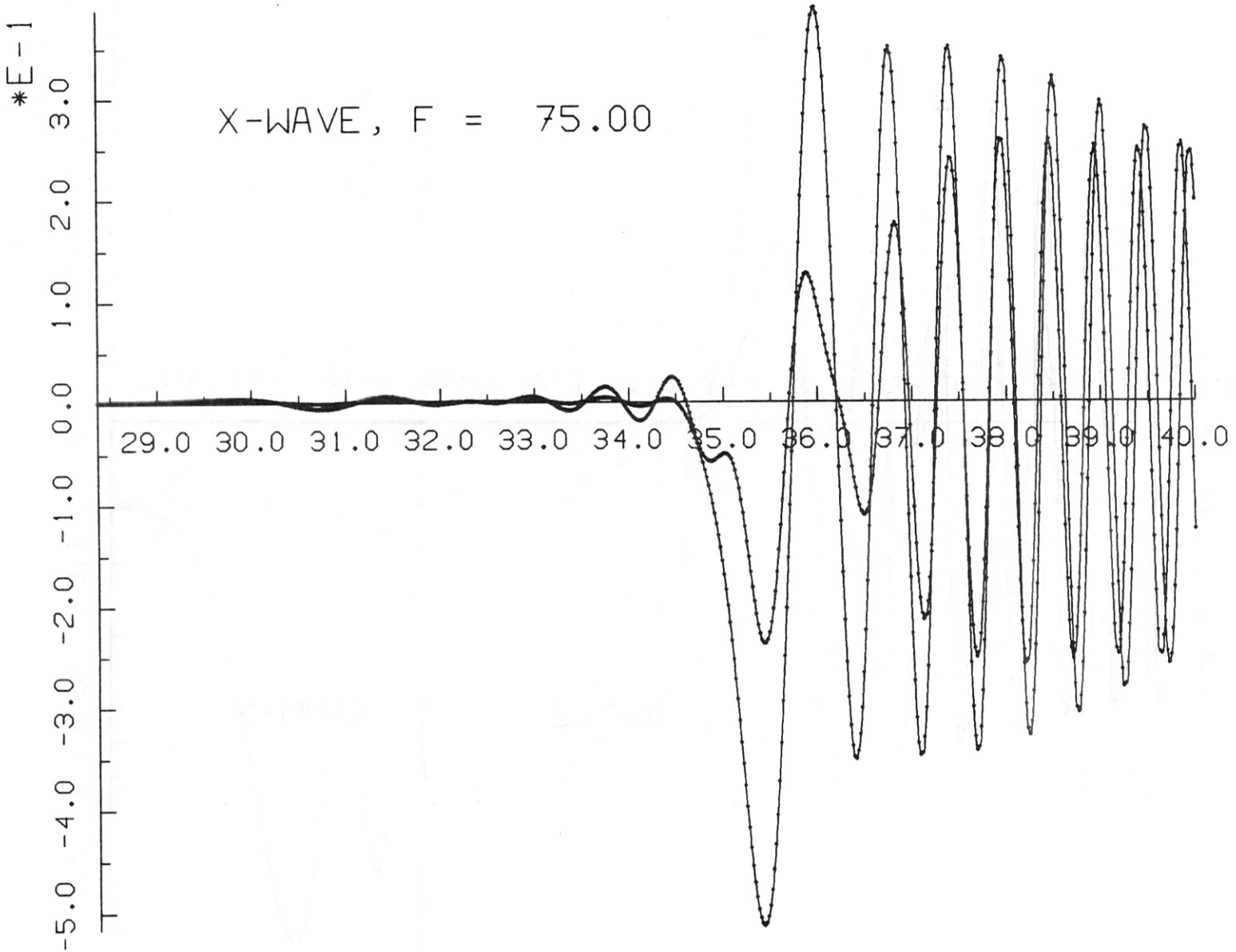
X-WAVE, F = 75.00
*E-1
3.0
2.0
1.0
0.0
-1.0
-2.0
-3.0
-4.0
-5.0
29.0
30.0
31.0
32.0
33.0
34.0
35.0
36.0
37.0
38.0
39.0
40.0

Fig. 7 b

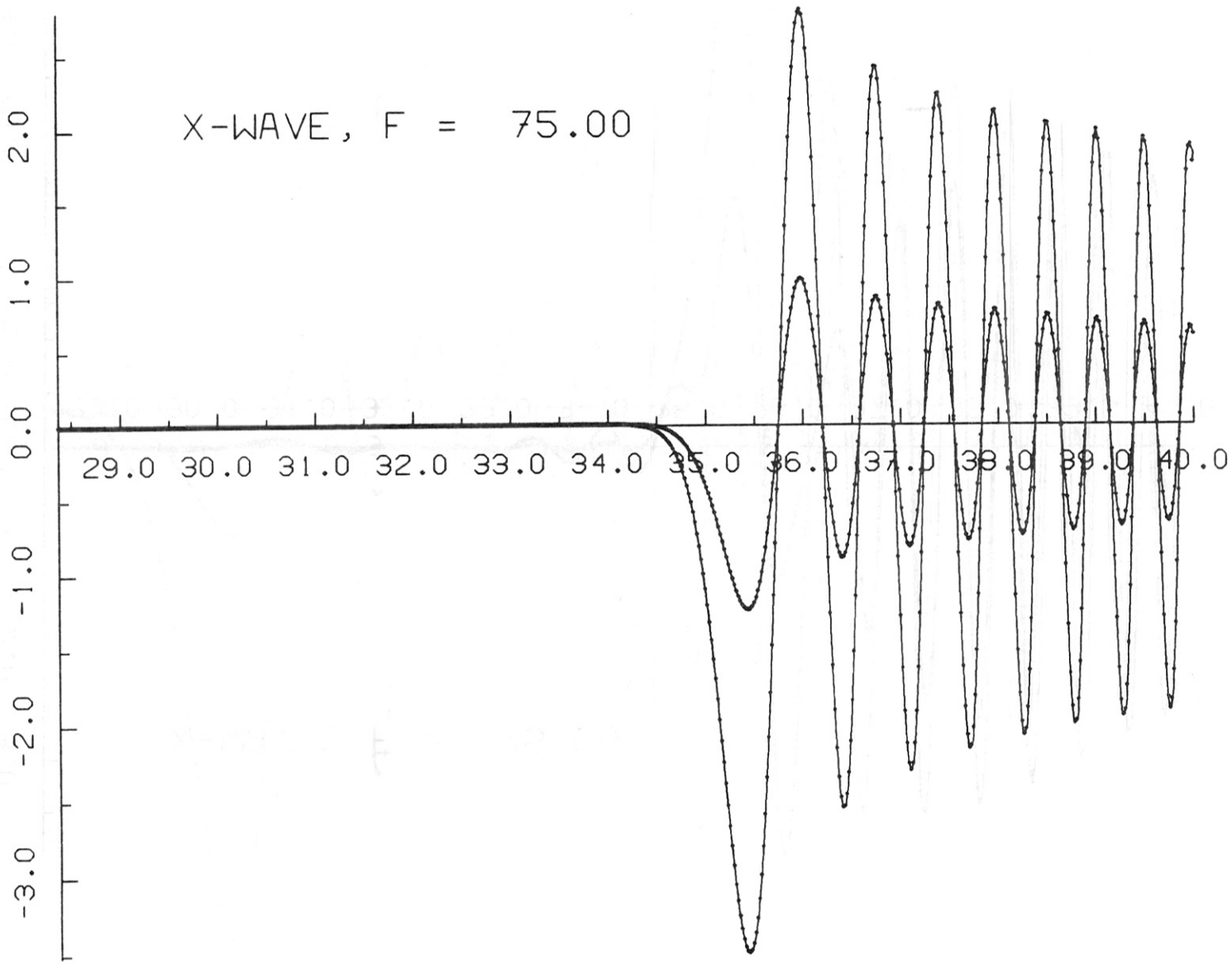
X-WAVE, F = 75.00
2.0
1.0
0.0
-1.0
-2.0
-3.0
29.0 30.0 31.0 32.0 33.0 34.0 35.0 36.0 37.0 38.0 39.0 40.0

Fig. 8 a

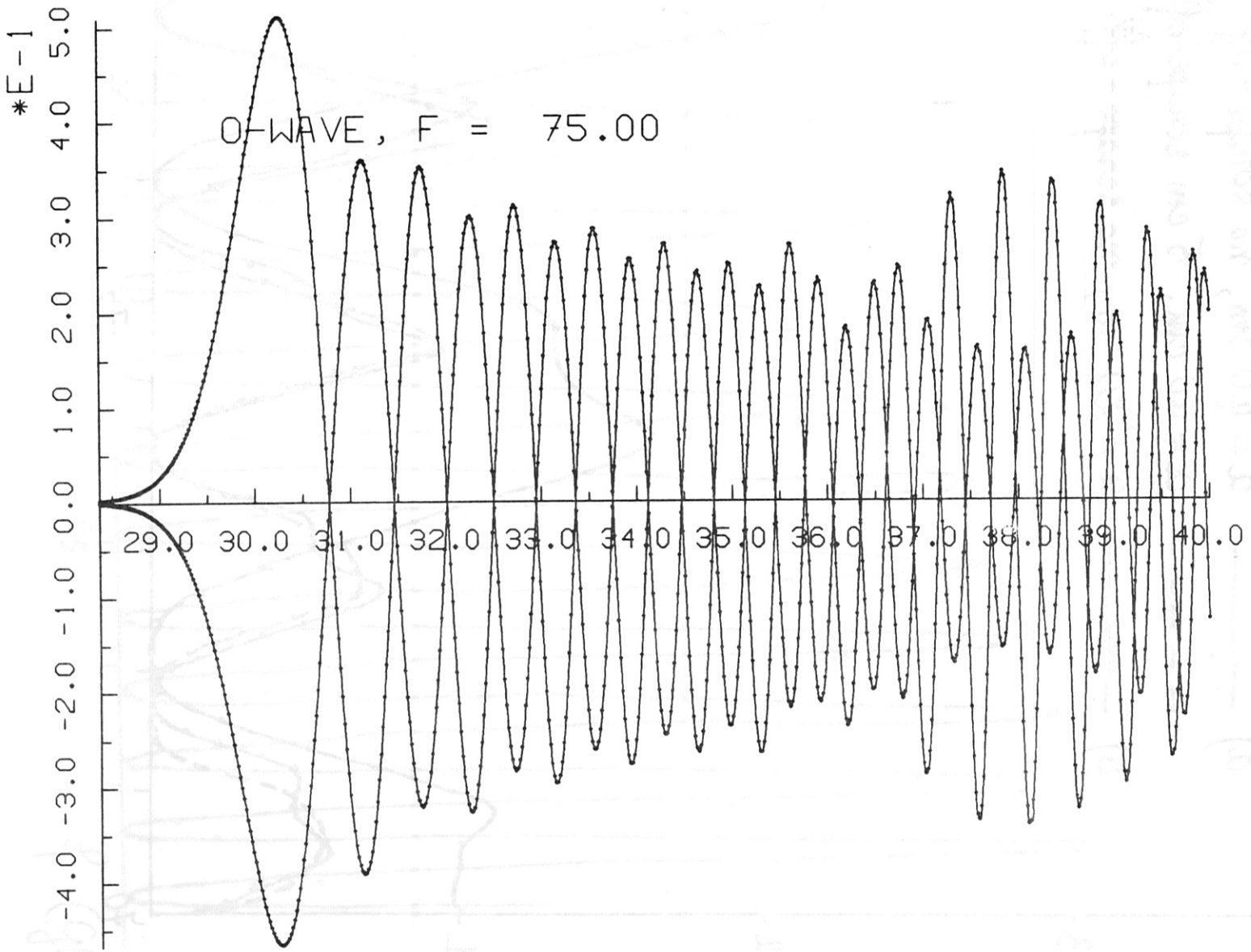
*E-1
5.0
4.0
3.0
2.0
1.0
0.0
-1.0
-2.0
-3.0
-4.0
O-WAVE, F = 75.00
29.0
30.0
31.0
32.0
33.0
34.0
35.0
36.0
37.0
38.0
39.0
40.0

Fig. 8b

Fig. 9

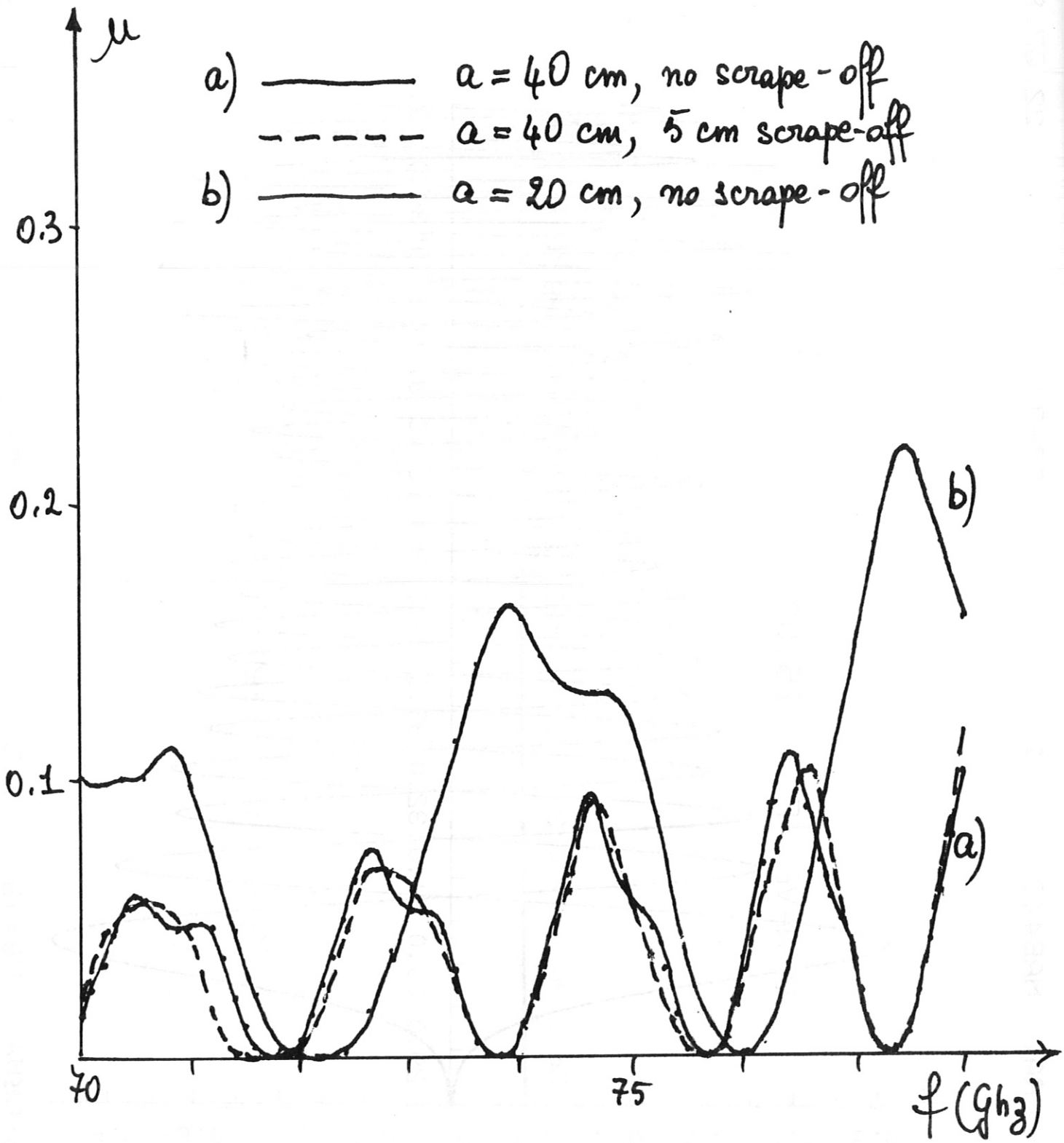
μ
a) ——— a = 40 cm, no scrape-off
- - - - - a = 40 cm, 5 cm scrape-off
b) ——— a = 20 cm, no scrape-off
0.3
0.2
0.1
b)
a)
70
75
f (Ghz)

Fig. 10

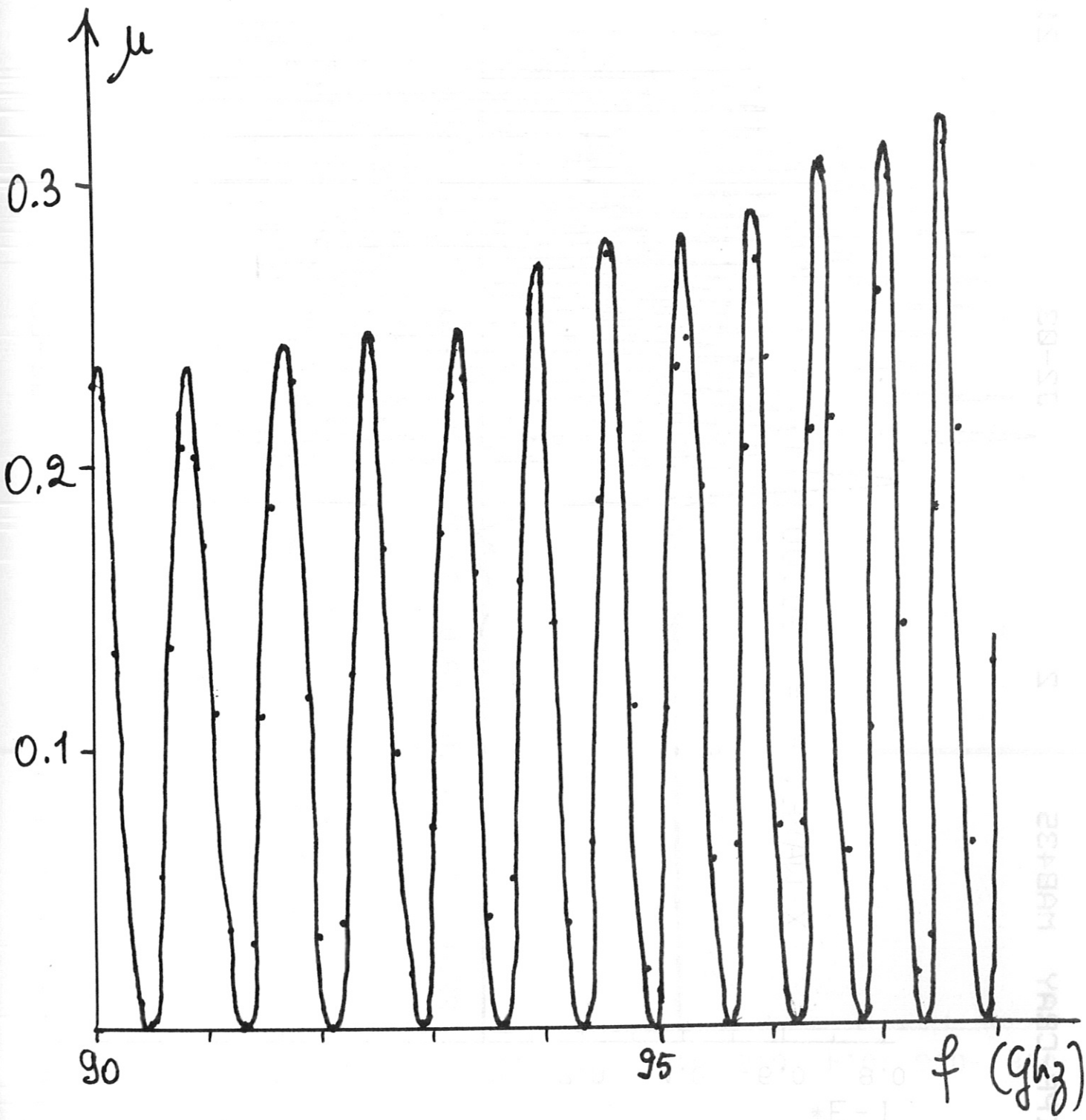

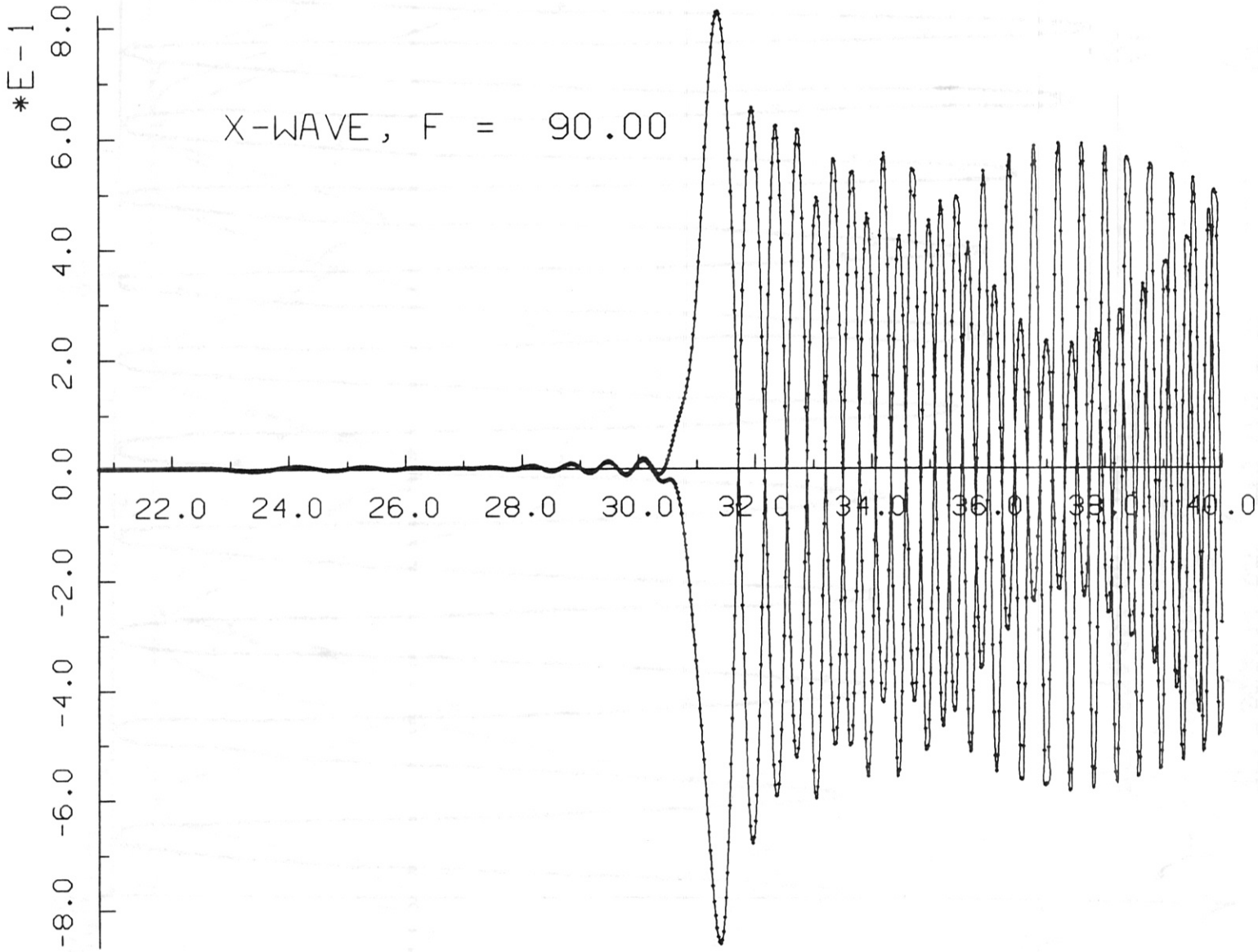
X-WAVE, F = 90.00
*E-1
8.0
6.0
4.0
2.0
0.0
-2.0
-4.0
-6.0
-8.0
22.0
24.0
26.0
28.0
30.0
32.0
34.0
36.0
38.0
40.0

Fig. 11a

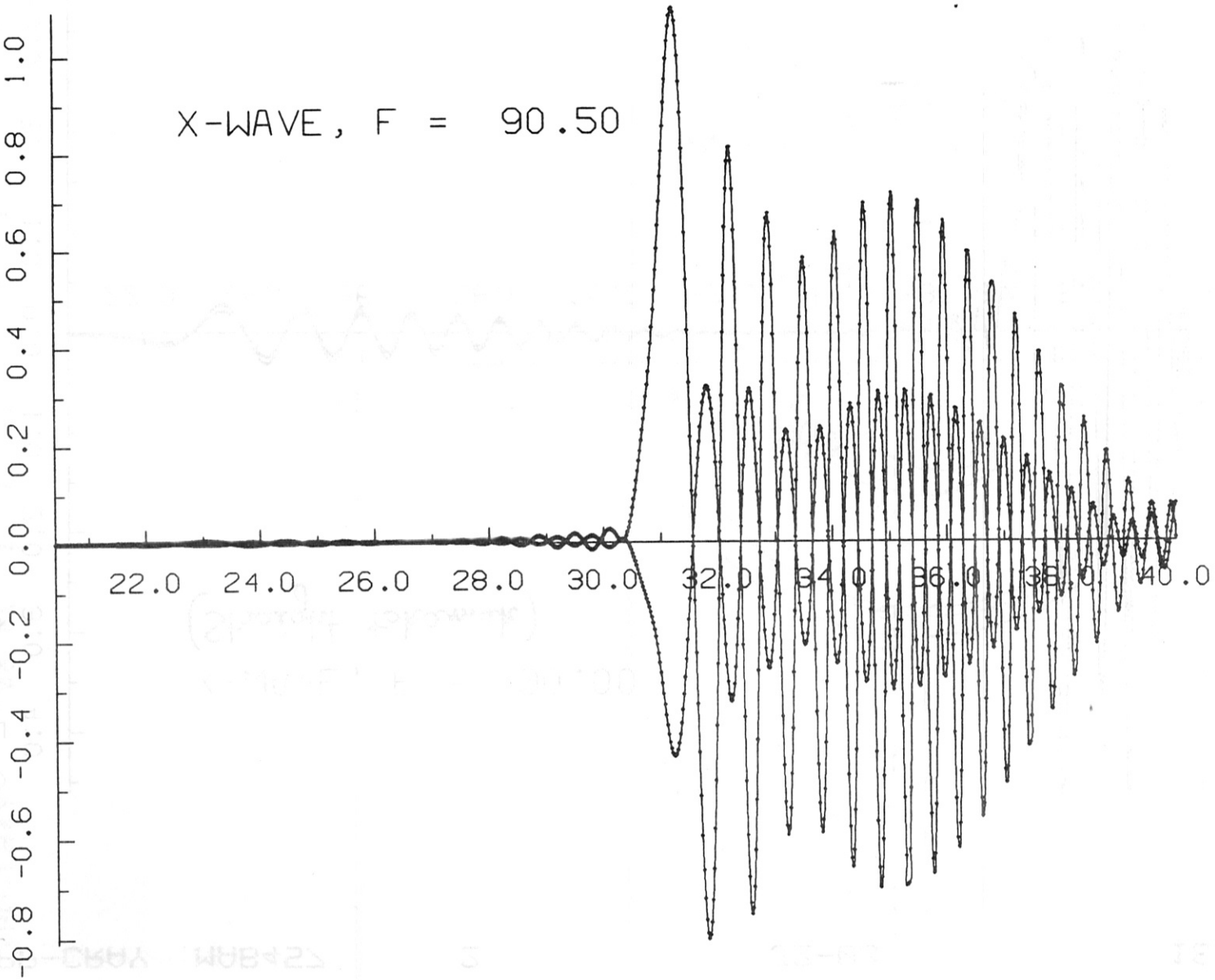
X-WAVE, F = 90.50
1.0
0.8
0.6
0.4
0.2
0.0
-0.2
-0.4
-0.6
-0.8
22.0
24.0
26.0
28.0
30.0
32.0
34.0
36.0
38.0
40.0

Fig. 11 b

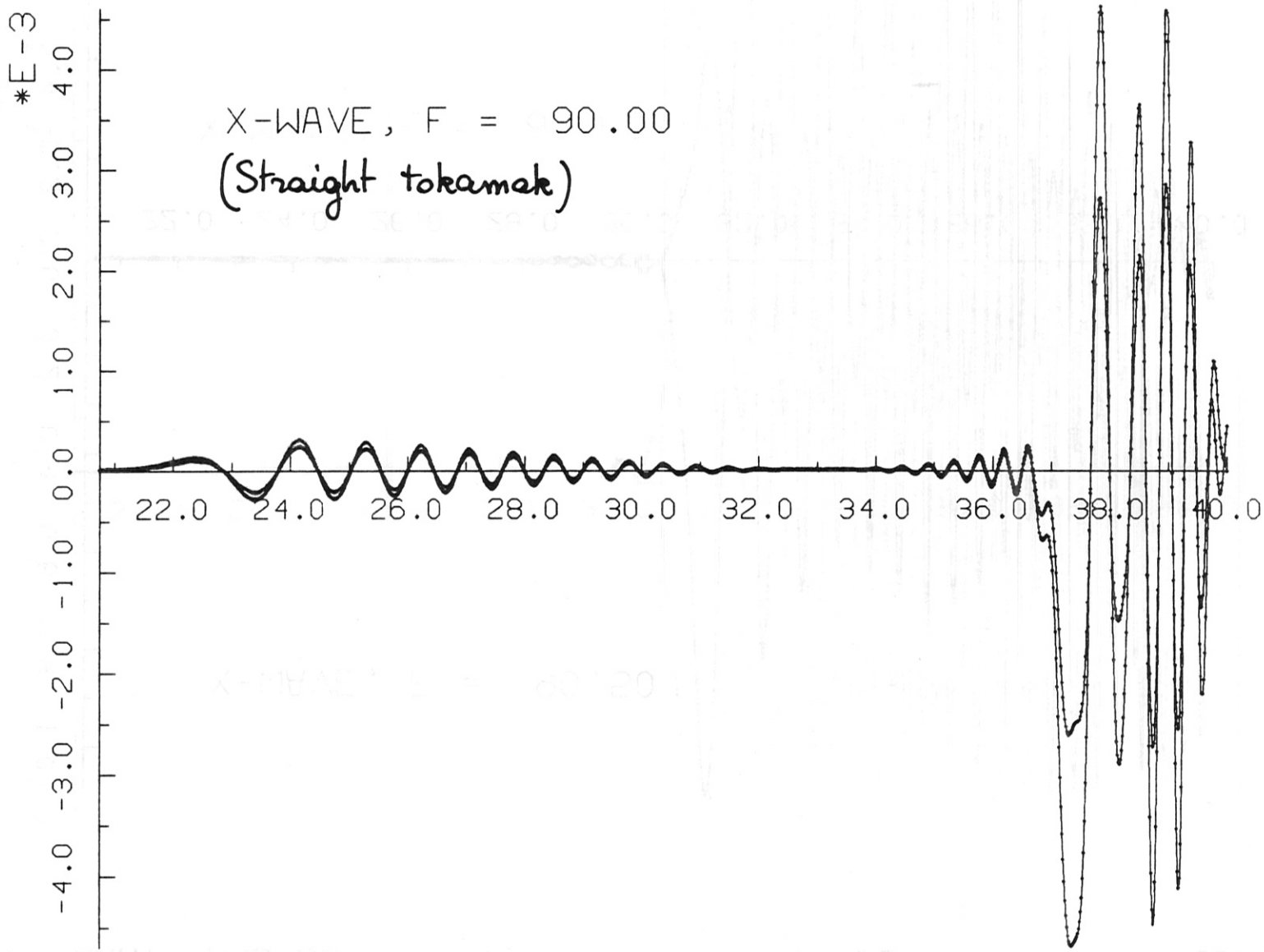
*E-3
4.0
3.0
2.0
1.0
0.0
-1.0
-2.0
-3.0
-4.0
X-WAVE, F = 90.00
(Straight tokamak)
22.0
24.0
26.0
28.0
30.0
32.0
34.0
36.0
38.0
40.0

Fig. 12

IPP-CRAY 08.86 17:12:47 MAB486 J2-03 001

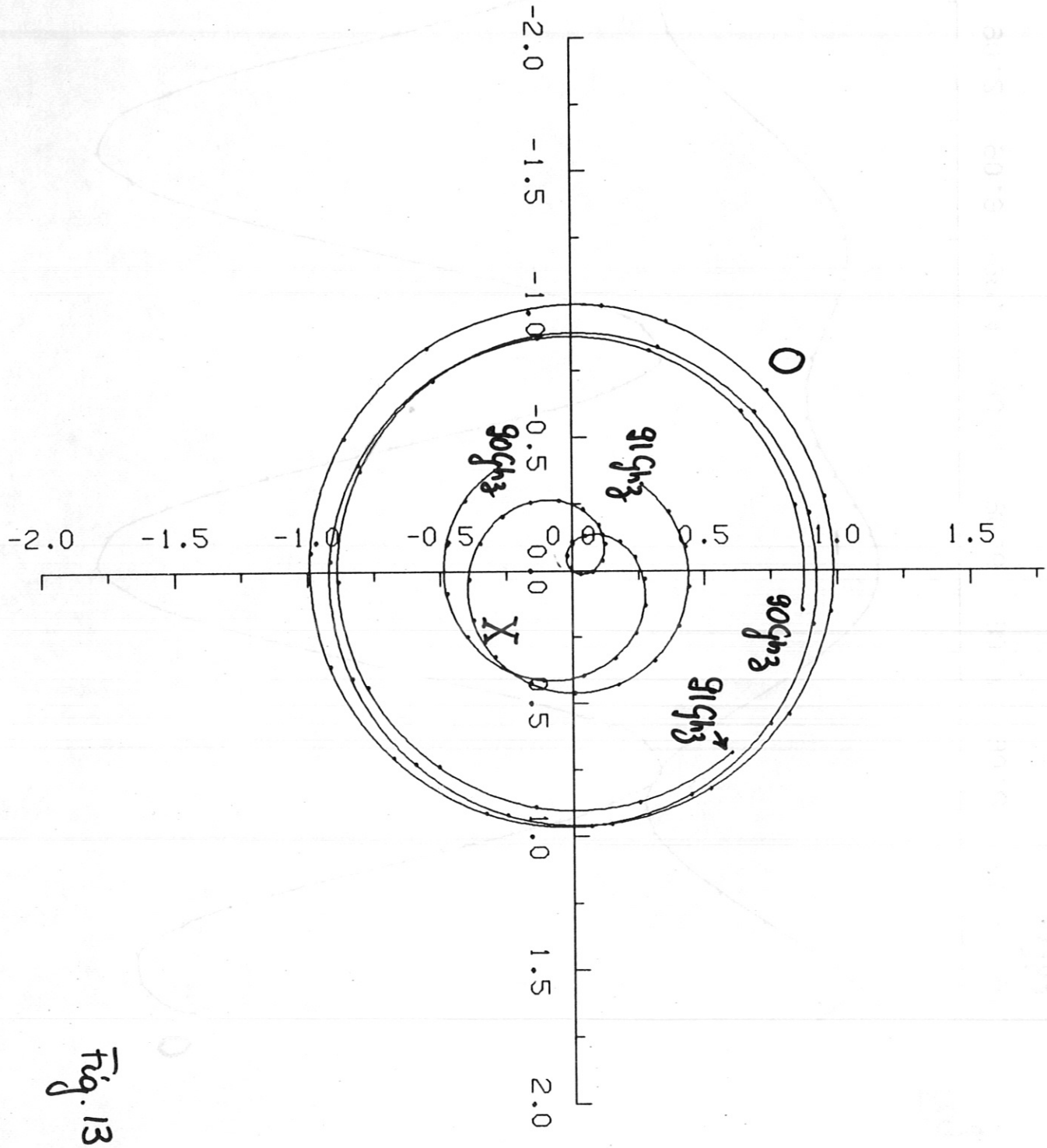

Fig. 13

IPP-CRAY 08.86 07:56:37 MAB488 J2-03 001
(a.u.)
0.0
1.0
2.0
3.0
4.0
5.0
6.0
90.0
90.1
90.2
90.3
90.4
90.5
90.6
90.7
90.8
90.9
91.0
GHz
O
X

Fig. 14